



OPEN

The catalytic performance of CuFe_2O_4 @CQD nanocomposite as a high-perform heterogeneous nanocatalyst in nitroaniline group reduction

Samin Naghash-Hamed, Nasser Arsalani¹✉ & Seyed Borhan Mousavi²✉

In this study, we fabricated an economical, non-toxic, and convenient magnetic nanocomposite of CuFe_2O_4 nanoparticles (NPs)/carbon quantum dots (CQDs) of citric acid via the co-precipitation method. Afterward, obtained magnetic nanocomposite was used as a nanocatalyst to reduce the ortho-nitroaniline (o-NA) and para-nitroaniline (p-NA) using a reducer agent of sodium borohydride (NaBH_4). To investigate the functional groups, crystallite, structure, morphology, and nanoparticle size of the prepared nanocomposite, FT-IR, XRD, TEM, BET, and SEM were employed. The catalytic performance of the nanocatalyst was experimentally evaluated based on the ultraviolet–visible absorbance to assess the reduction of o-NA and p-NA. The acquired outcomes illustrated that the prepared heterogeneous catalyst significantly enhanced the reduction of o-NA and p-NA substrates. The analysis of the absorption showed a remarkable decrease for ortho-NA and para-NA at $\lambda_{\text{max}} = 415 \text{ nm}$ in 27 s and $\lambda_{\text{max}} = 380 \text{ nm}$ in 8 s, respectively. The constant rate (k_{app}) of ortho-NA and para-NA at the stated λ_{max} was $8.39 \times 10^{-2} \text{ s}^{-1}$ and $5.48 \times 10^{-1} \text{ s}^{-1}$. The most highlighted result of this work was that the CuFe_2O_4 @CQD nanocomposite fabricated from citric acid performed better than absolute CuFe_2O_4 NPs, since nanocomposite containing CQDs had a more significant impact than copper ferrite NPs.

Nanocatalysis is among the ultimate fascinating catalysis category, which has important advantages incorporated with both heterogeneous and homogenous catalysis¹. The rapid development of chemical industries leads to an increasing number of aromatic pollutants that significantly threaten nature and the environment. Finding an effective way to control aromatic pollutants requires scientific and technological importance to be grown up. Innumerable research studies on the environmental issues of aromatic pollutants have attempted to pay considerable attention to water-soluble aromatic dyes and nitro compounds. Catalytic reduction of aromatic compounds, which are water-soluble by heterogeneous catalysts due to their easy usage, high efficiency, profitability, and low cost, has received much attention. Moreover, catalytic reduction and conversion of nitroaromatic compounds to valuable amino-based compounds have been widely reported. According to the reduction reaction model, such as the reduction of chemical aromatic dyes or nitro compounds by a reductant agent of NaBH_4 , qualitative assessment and comparison of different catalysts based on their activities can also be achieved^{2–5}. In recent years, the use of dyestuff outcomes and aromatic pollutants have risen due to industrial modification and technological advancement. Also, discharging the organic pollutants directly into the aqueous environment severely affects aquatic and human life. Many industries, including textile, plastic, cosmetics, and leather, unload their squander into the water resources, which could influence the environment and aquatic life⁶. Nitroaromatic compounds are classified as environmental pollutants since they have been released into the atmosphere⁷. The ortho-nitroaniline (o-NA) and para-nitroaniline (p-NA) have been reported as highly toxic pollutants in wastewater by the United States Environmental Protection Agency (US-EPA). In order to remove or lessen the impact of pollution from water sources, various approaches have been revealed, like adsorption, microbial degradation, photocatalysis,

¹Research Laboratory of Polymer, Department of Organic and Biochemistry, Faculty of Chemistry, University of Tabriz, Tabriz, Iran. ²J. Mike Walker '66 Mechanical Engineering Department, Texas A&M University, College Station, TX, USA. ✉email: arsalani@tabrizu.ac.ir; seyedborhanm@gmail.com; borhanm@tamu.edu

catalysis, electrochemical treatment, and Fenton's method^{18,9}. Among the mentioned methods, catalysis is the greater way to eliminate pollution due to its properties such as time-saving, high satisfaction, and economical.

Recently, nanoparticles have been used in various applications such as heat transfer^{10–14}, lubrication^{15–17}, CO₂ capture^{18–20}, textile manufacturing^{21–25}, photocatalyst, water treatment systems²⁶, and catalysis²⁷. Magnetic ferrites are used in fundamental research fields due to their electrical, magnetic, chemical/thermal stability properties and spinal properties (MFe₂O₄; M = Ni, Co, Fe, Cu, Zn, etc.)^{28,29}. The chance of synthesizing the nano ferrites in the form of solid solutions can unclothe the proper way to adapt and alter their properties for vast applications^{30,31}. Nano-crystalline magnetic ferrite of (CuFe₂O₄) has been fabricated by different methods, such as solid-state reaction³², co-precipitation³³, hydrothermal³⁴, solution auto combustion³⁵, and sol–gel³⁶. The intriguing outcomes revealed that the prepared samples' surface area, magnetic parameter, particle size, crystallites, and catalytic properties were changed based on preparation techniques³⁷.

Carbon is an adjustable element that could produce various hybridization modes, including sp, sp², and sp³. This makes a broad spectrum of allotropes from the softest to the hardest materials³⁸. Much theoretical to practical efforts have focused on carbon nanostructures progressing in a broad range in terms of application. Carbon-based dots (CDs) can be classified into CQDs (carbon quantum dots), GQDs (graphene quantum dots), and carbon nanodots (CNDs) based on their carbon arrangement and crystal structure^{39,40}. Carbon quantum dots were randomly unearthed throughout the purification stages of carbon nanotubes in 2004⁴¹. Carbon quantum dots have a broad range of utilization due to their remarkable characteristics, such as low toxicity, higher fluorescence properties, intriguing biocompatibility, greater chemical stability, and electron transfer efficiency⁴².

It is claimed that the reduction product of o-NA and p-NA is o-phenylenediamine (o-PDA) and p-phenylenediamine (p-PDA), respectively, which have been widely used in different fabrication, namely pharmaceuticals, polymers, dyes, surfactants, and pesticides⁴³. Edison et al.⁴⁴ studied the ortho-nitroaniline reduction by adding NaBH₄ and Ag nanoparticles (NPs) fabricated from Tamarindus indica seed. They observed that the green-synthesized Ag NPs had an excellent performance in reducing o-NA with a constant rate of about $2.43 \times 10^{-3} \text{ s}^{-1}$, which was greater than other synthesized Ag NPs as a candidate catalyst. Baran et al.⁴⁵ examined the o-NA reduction with a practical, highly active, and easily recoverable hybrid Pd/CoFe₂O₄/chitosan nanocatalyst. The outcomes represented that the nanocatalyst could convert the o-NA to o-PDA in 65 s, which is an excellent result due to its short reaction time. Gupta et al.⁴⁶ analyzed the impact of gold NPs by synthesizing the shape-selective Au NPs via microwave-assisted technique in 6 min. They noticed that gold nanocubes could reduce the para-NA in 6 min and showed great reusability for at least four cycles. The shape dependency of nanocatalyst was further confirmed in their study. Liu et al.⁴⁷ assessed the persuasive catalyst for reducing p-NA by KBH₄ with a prepared gold nanoflowers (GNFs) catalyst. The outcomes demonstrated that GNFs catalysts had an efficacious influence on the reduction of p-NA. Different nanocatalysts in shapes, including dog bone, rod, and spherical shapes, were fabricated from gold (Au) by Jiji et al.⁴⁸. They concluded that the gold NPs with a rod shape had a superior effect rather than spherical and dog bone shape NPs. In addition, the reaction time of 42, 122, and 230 s declared for rod, dog bone, and spherical shape, respectively. Revathi et al.⁴⁹ studied the nanocomposite performance by synthesizing the facile and low-cost Cu–CuO nanocomposite to reduce the nitroarenes. They observed that prepared (Cu–CuO) nanocomposite revealed greater catalytic enhancement to reduce the p-NA into the p-PDA rather than Cu and CuO.

According to the conducted literature review, the preponderance of examinations in the aforementioned area announces a positive impact on the catalytic effect of different catalysts with various shapes on the reduction of o-NA and p-NA. Based on the investigations in the field of reduction, comprehensive examinations have been carried out using expensive and rare materials, such as silver and gold. Also, using several materials to prepare nanocomposites is not economically friendly, and it causes much time to fabricate nanocatalysts. Consequently, in this article, for the first time to the best of our knowledge, CuFe₂O₄@CQD nanocomposite was successfully synthesized as a catalyst from citric acid and used to reduce organic pollutants of o-nitroaniline and p-nitroaniline.

We planned and fabricated a novel and economical magnetic CuFe₂O₄@CQD nanocomposite as a nanocatalyst via the co-precipitation method. The impact of the nanocatalyst on the reduction of o-NA and p-NA with a reductant of NaBH₄ was analyzed. To evaluate the reusability of the nanocatalysts, magnetic catalyst NPs were separated from the solution by an external and robust magnet and were reused for up to at least 6 recycles.

Experimental part

Chemicals. Citric acid (HOC(CO₂H) (CH₂CO₂H)₂), sodium borohydride (NaBH₄), para-nitroaniline (C₆H₆N₂O₂), ethanol (C₂H₅OH), sodium hydroxide (NaOH), and ortho-nitroaniline (C₆H₆N₂O₂) were commercially purchased from Merck.

Scrutinizing the functional groups of fabricated CQDs and nanocomposite of CuFe₂O₄@CQD were employed by Fourier transform infrared spectroscopy [FT-IR, Nexus Model Infrared spectrophotometer (Nicolet Co, USA)]. A SEM (Carl Zeiss 1430VP L, Germany) and TEM (EM 208S, Philips, Netherland) were applied to illustrate nanocomposite morphology and size distribution. To obtain the crystal structure and crystallite size of nanoparticles at room temperature, X-ray diffraction (XRD, PW1730, Philips, The Netherlands) with Cu-Kα ($\lambda = 1.54056 \text{ \AA}$) radiation was performed. The pattern was analyzed with XRD, recorded with a step size of 0.05°/1 s, and between the angular radiuses of 10–80° (2θ). To demonstrate the catalytic property of nanocomposite, UV–visible absorption spectra (UV–Vis, Specord 250, Analytik Jena) was utilized. The magnetic stirrer (Fan Azma Gostar, Iran) was utilized for dissolving the solutions to intercept the agglomeration. A centrifuge (Hettich Centrifuge EBA III) was exploited to help the separation process. Physical adsorption and desorption of N₂ at 77 K with BELSORP MINI II device was used to measure the BET surface area and pore volume distribution of BJH of the synthesized sample. To evaluate the magnetic properties of the synthesized samples in a magnetic field of ± 15 kOe, a vibrating sample magnetometer (VSM-model MDKF-FORC/VSM, Megnatis-Daghigh-Kashan

Co., Kashan, Iran) was utilized. The magnetization as a function of temperature (M – T curves) was recorded in the temperature range of 10–380 K.

Synthesis of copper ferrite nanoparticles. CuFe_2O_4 NPs were synthesized via the facile one-step hydrothermal method. Initially, 0.574 g of tetrasodium EDTA salt as a chelator was dispersed in 50 mL of deionized (DI) water for 10–15 min in an ultrasonic bath cleaner. Then, the stoichiometric amount of 3.24 g of anhydrous FeCl_3 and 1.35 g of $\text{CuCl}_2 \cdot 2\text{H}_2\text{O}$ were added to the desired solution under constant stirring speed. The alkaline solution, prepared by adding 17.7 g of granular sodium hydroxide per 100 mL of water, was added dropwise to the solution using a syringe (during the reaction, the pH of the reaction was continuously monitored using a pH meter). When the pH reached 10–11, the solution was poured into a Teflon autoclave at 185 °C for 15 h. After the completion of the reaction by a strong external magnet, the magnetic sediment was separated and washed several times with ethanol and distilled water. Finally, the prepared brown sediment was dried at 60 °C for approximately 3–4 h.

Facile fabrication of carbon quantum dots (CQDs) from citric acid. Fabricating yellowish carbon quantum dots from citric acid is shown in Fig. 1. To prepare quantum dots of carbon, about 2.00 g of citric acid (CA) was melted at 200 °C under continuous magnetic stirring. The prepared NaOH solution (1.00 g of NaOH added to the 100 cc of absolute ethanol) was steadily poured into the CA. When the precipitate formed, the resulting liquid was centrifuged at 7 rpm. Ultimately, the precipitate was dried in an oven at 50 °C for 4 h till the yellowish powder was obtained. Acquired CQDs under UV light had a fluorescence property.

Fabrication of CuFe_2O_4 @CQD nanocomposite. CuFe_2O_4 @CQD nanocomposite was fabricated via a simple co-precipitation method with a weight ratio of 2:1. Figure 2 illustrates the schematic of the preparation procedure. In order to fabricate the nanocomposite, 0.105 g of CuFe_2O_4 and 0.058 g of CQDs were poured into the 15 mL of ethanol; then, they were dissolved for 15 min. Subsequently, the mixture was heated at 70 °C, incorporated under the argon noble gas, and stirred perfectly under stirring for 5 h into an oil bath. The brown resulting precipitate was detached via an external magnet and alternately washed with deionized (DI) water and ethanol. Finally, it was dried in the hot oven for 4 h at 80 °C. Consequently, CuFe_2O_4 @CQD nanocomposite was fabricated and ready to use as a reduction reaction catalyst.

Catalytic performance evaluation. The catalytic reduction examination was employed in the omission and presence of catalyst into a quartz cuvette with a total volume of 3.50 mL and 1 cm path length. This evaluation was conducted to reduce o-nitroaniline and p-nitroaniline as a model of the organic nitro compounds in the presence of NaBH_4 . For a typical investigation, 20 mg of o-NA and p-N were separately dissolved in 100 mL of DI water for 20 min. Afterward, 5 mL of the prepared nitro mixture, 100 mg of NaBH_4 as a reducing agent, and 3.5 mg of nanocomposite as a catalyst were subsequently added to the testing tube. In the end, 100 μL of the resulting solution was transferred expeditiously into the quartz cuvette, and its absorption was measured once a few seconds till the color of the solution was completely altered.

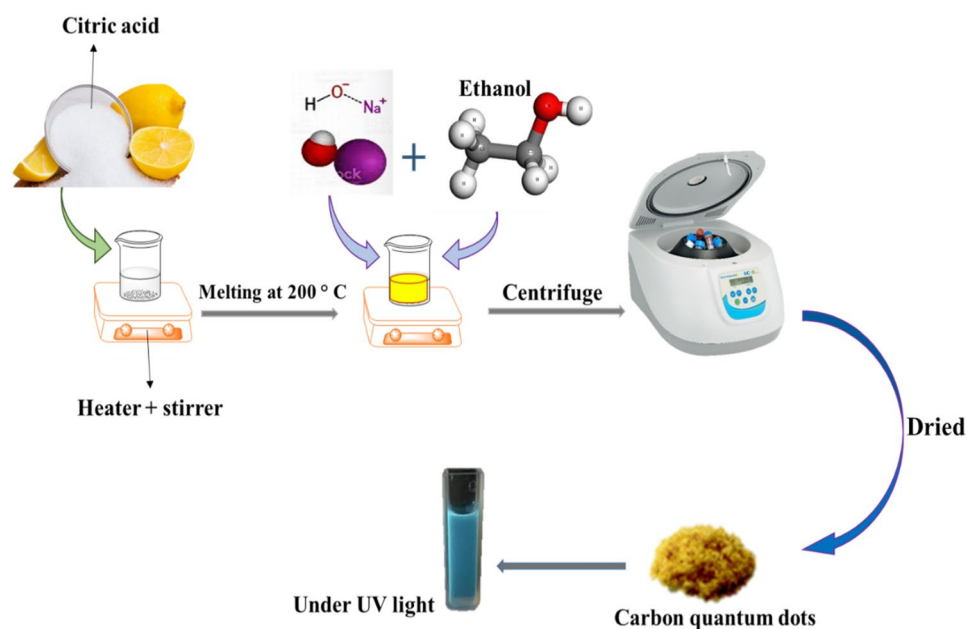


Figure 1. Synthesis of yellowish carbon quantum dots from citric acid.

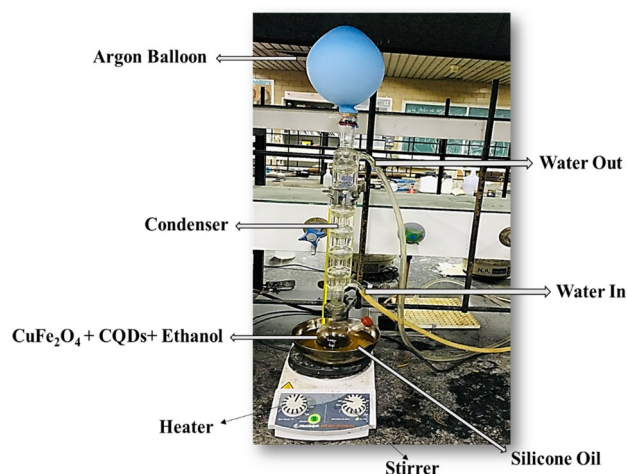


Figure 2. Representation of co-precipitation technique applied for fabrication of $\text{CuFe}_2\text{O}_4@\text{CQD}$ nanocomposite.

Results and discussion

Characterization. Figure 3a shows the FT-IR analysis of the $\text{CuFe}_2\text{O}_4@\text{CQD}$ nanocomposite. It is observable in Fig. 3a, that the strong band at approximately 572 cm^{-1} was ascribed to the deformation of Fe–O in octahedral sites, displaying the functional groups of CuFe_2O_4 into the $\text{CuFe}_2\text{O}_4@\text{CQD}$ nanocomposite⁵⁰. The observed bands at 1388 cm^{-1} and 1595 cm^{-1} corresponded to the metal–OH (Fe–OH and Cu–OH) bending vibration, respectively^{51,52}. The intense peak at 1014 cm^{-1} depicted the FeOOH bond. The broad absorption from 3700 to 3400 cm^{-1} corresponded to the O–H stretching vibration group. This stretching vibration belonged to the $\text{CuFe}_2\text{O}_4@\text{CQD}$ and was assigned to the occupancy of water molecules that could exist on their surfaces⁵³. It is noteworthy that the presence of CQDs in the structure of the considered nanocomposite caused an overlap that enhanced the peak intensity and decreased it compared to the CuFe_2O_4 NPs peaks reported in previous work⁵⁴. Meanwhile, some of the peaks disappeared in the FT-IR of the nanocomposite.

The seen IR band in 3400 cm^{-1} in Fig. 3b was ascribed to the CQDs of citric acid, which was attributed to the attendance of the hydroxyl (R–OH) group in the structure of citric acid⁵⁵. As can be seen, the peak at 1728 cm^{-1} was allocated to the carbonyl groups (C=O bond) on the carbon quantum dots⁵⁶. The vibrational band of CH_2 and the stretching peak of C–OH are seen in 621 cm^{-1} and 1082 cm^{-1} , respectively⁵⁷. The intense peaks at 1385 cm^{-1} and 1585 cm^{-1} depicted the symmetric and anti-symmetric vibration of the (CO_2^-) group, sequentially, which

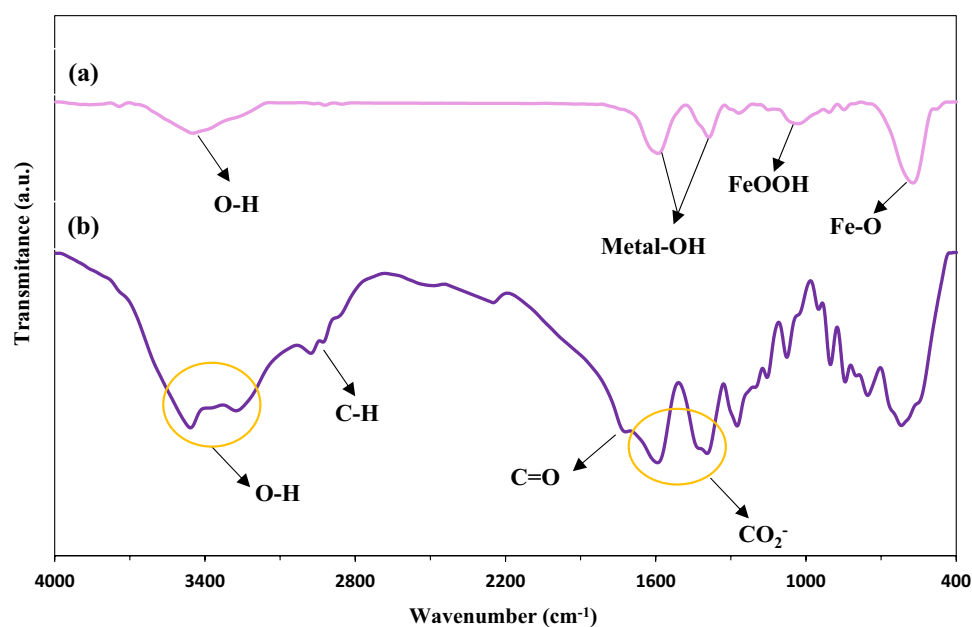


Figure 3. FT-IR spectrum of (a) $\text{CuFe}_2\text{O}_4@\text{CQD}$, (b) CQDs of citric acid.

was consistent with the presence of the acidic group on the surface of the quantum dots of carbon^{58,59}. The peak at 2970 cm^{-1} corresponded to the C–H band⁶⁰.

The X-ray diffraction pattern of $\text{CuFe}_2\text{O}_4\text{@CQD}$ nanocomposite is represented in The peak demonstrated around $2\theta = 24^\circ$ was not recognized in the X-ray diffraction pattern of CuFe_2O_4 NPs, which was demonstrated as the CQDs peak.

Figure 4 can be seen that the XRD pattern for the sample has prime 5 intense peaks at $2\theta = 30.12^\circ, 35.84^\circ, 43.99^\circ, 57.74^\circ,$ and 62.79° corresponded to (112), (211), (312), (112), and (400), consecutively⁶¹. Every single diffraction of the fabricated sample is in high approval of the JCPDS card (34-0425), illustrating the tetragonal structure of copper ferrite NPs. Furthermore, the peaks seen at $2\theta = 37.39^\circ, 49.59^\circ,$ and 54.14° corresponded to the (*111), (*-202), and (*020), indicating the monoclinic CuO phase plane (JCPDS No. 80-1916)⁶². In terms of Fe^{3+} and Cu^{2+} complex constants, the presence of CuO may be reasonable. The complex constant of Fe^{3+} ($\log \beta = 20.19 \pm 0.02$) is larger than that of Cu^{2+} ($\log \beta = 8.08$), so Fe^{3+} complexes should be more stable than Cu^{2+} . Therefore, Cu^{2+} agglomerates with NaOH and finally forms CuO ^{53,63}. Some secondary impurities, such as Fe_2O_3 were still found, peaks seen at $2\theta = 33.69^\circ$ and 64.24° , which may be attributed to the insolubility of FeO , are in a good acceptance of the JCPDS card (33-0664)⁶³. The strong peak at $2\theta = 40.97^\circ$ is indexed to the Cu element⁶⁴.

To enumerate the crystallite size of $\text{CuFe}_2\text{O}_4\text{@CQD}$ nanocomposite, the Debye–Scherrer's formula could be calculated as follows^{65,66}:

$$D = \frac{K\lambda}{\beta \cos\theta} \quad (1)$$

where D_{avg} , K , λ , β , and θ are ascribed to the average crystallite size of NPs (nm), the wavelength of the X-ray pattern, the full width at the half apex of the maximum diffraction (FWHM), and the Bragg angle. This peak corresponded to the reflection of the (002) plane of carbon quantum dots, confirming the accurate fabrication of nanocomposite. Moreover, it is obvious that the sharp peaks denoted the crystallite and purity nature of fabricated samples, and the broad peak of CQD represented the amorph structure⁶⁷. According to the FWHM crystal plane (211), based on the Scherrer equation, the crystallite size of nanoparticles was calculated to be about 14.30 nm. The peak demonstrated around $2\theta = 24^\circ$ was not recognized in the X-ray diffraction pattern of CuFe_2O_4 NPs, which was demonstrated as the CQDs peak.

The surface structure, morphology, shape, and crystallite of $\text{CuFe}_2\text{O}_4\text{@CQD}$ nanocomposite were analyzed using SEM and TEM (Fig. 5). Moreover, acquired nanocomposite depicted a mixture of cubic and spherical structures due to synthesizing techniques⁶⁶. The $\text{CuFe}_2\text{O}_4\text{@CQD}$ nanocomposite had a diameter range of 78.5 nm. It becomes apparent that pictures depicted agglomeration due to the two dominant reasons. The CuFe_2O_4 NPs have a magnetic property, and carbon quantum dots tend to build new larger structures, so they stay in one place to get bigger and are seen as agglomeration. The outcome of this occurrence is that the smallest particles accumulate at higher temperatures and form large particles that are heterogeneous in size⁶⁷. The EDS-mapping pictures of the nanocatalyst are illustrated in Fig. 6, which confirms the elemental composition of $\text{CuFe}_2\text{O}_4\text{@CQD}$. Cu , O , C , and Fe elements were well dispersed into the $\text{CuFe}_2\text{O}_4\text{@CQD}$ nanocomposite. The EDX spectrum of the $\text{CuFe}_2\text{O}_4\text{@CQD}$ nanocomposite is exhibited in Fig. 7. In Fig. 7, the presence of C (citric acid), Cu , Fe , and O elements in the nanocomposite structure is confirmed.

Corresponding magnetic measurements of $\text{CuFe}_2\text{O}_4\text{@CQD}$ nanocomposite, which were performed in the magnetic field in the range of -15 to $+15$ kOe (M – H hysteresis loop), proved their satisfactory saturation magnetization (M_s) and favorable superparamagnetic properties (Fig. 8). The M_s value of CuFe_2O_4 NPs and $\text{CuFe}_2\text{O}_4\text{@CQD}$ nanocomposite was 25.68 emu g^{-1} and 20.27 emu g^{-1} without observing apparent remanence and coercivity, respectively. The CuFe_2O_4 NPs have a higher saturation magnetization than $\text{CuFe}_2\text{O}_4\text{@CQD}$

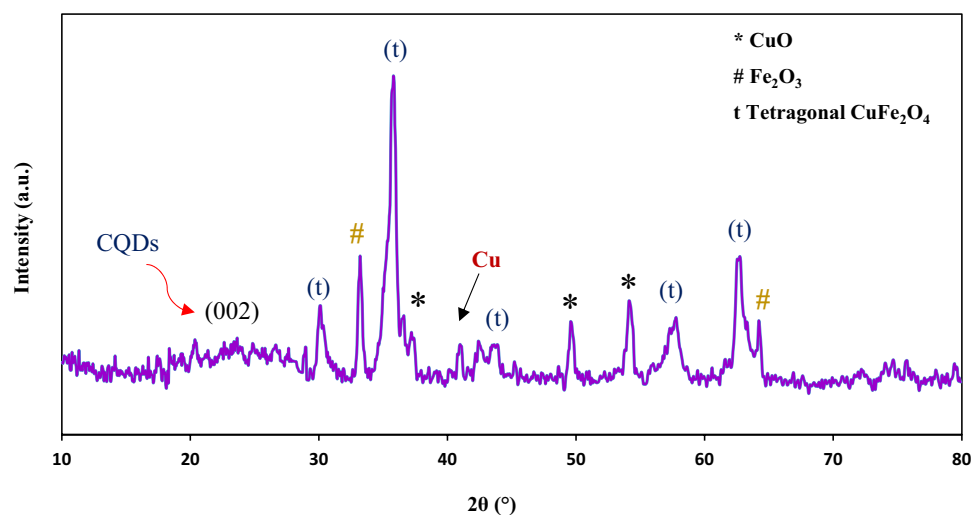


Figure 4. X-ray diffraction pattern of $\text{CuFe}_2\text{O}_4\text{@CQD}$ nanocomposite.

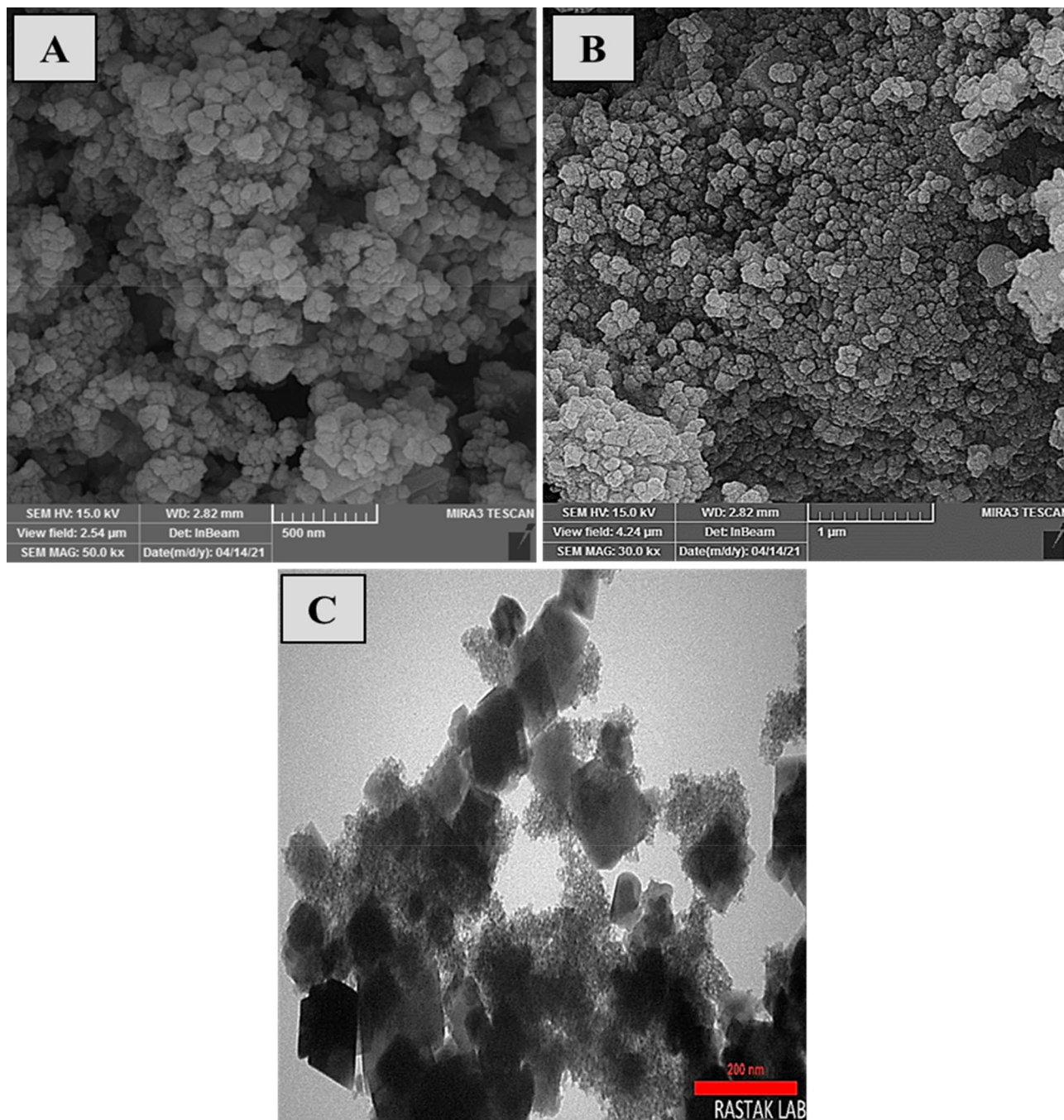


Figure 5. (A, B) SEM, (C) TEM images of $\text{CuFe}_2\text{O}_4@\text{CQD}$ nanocomposite.

nanocomposite. Such NPs can be rapidly assembled by an external magnetic field, providing multifunctional properties for separation and reduction processes. Because the average particle size of samples was less than 20 nm and showed reversible hysteresis curves with negligible retention and coercivity, the sample could exhibit superparamagnetic behavior. The H_c for CuFe_2O_4 NPs and $\text{CuFe}_2\text{O}_4@\text{CQD}$ nanocomposite were 0.064 Oe and 0.7 Oe, sequentially. It has been reported that the lower magnetization in nanoparticles is due to surface spin caused by competitive antiferromagnetic interactions⁶⁸. Lower magnetization can also be caused by the unsaturation of small arbitrarily dispersed particles that exhibit high crystal magnetic anisotropy. Other reasons were considered to justify the lower magnetization in nanoparticles, such as creating a passive magnetic layer, spin glass properties, and irregular cation distribution on the surface of nanoparticles⁶⁹.

Table 1 demonstrates the BET/BJH parameters of $\text{CuFe}_2\text{O}_4@\text{CQD}$ nanocomposite and CuFe_2O_4 nanoparticles. Based on the acquired features, $\text{CuFe}_2\text{O}_4@\text{CQD}$ nanocomposite has $29.5 \text{ m}^2/\text{g}$ of surface area, $0.04 \text{ cm}^3/\text{g}$ of pore volume, and 5.67 nm of mean pore diameter, revealing its nanoporous associated with significant accessible surface area. The free surface area of $110.6 \text{ m}^2/\text{g}$ and pore volume of $0.25 \text{ cm}^3/\text{g}$ disclose the considerable

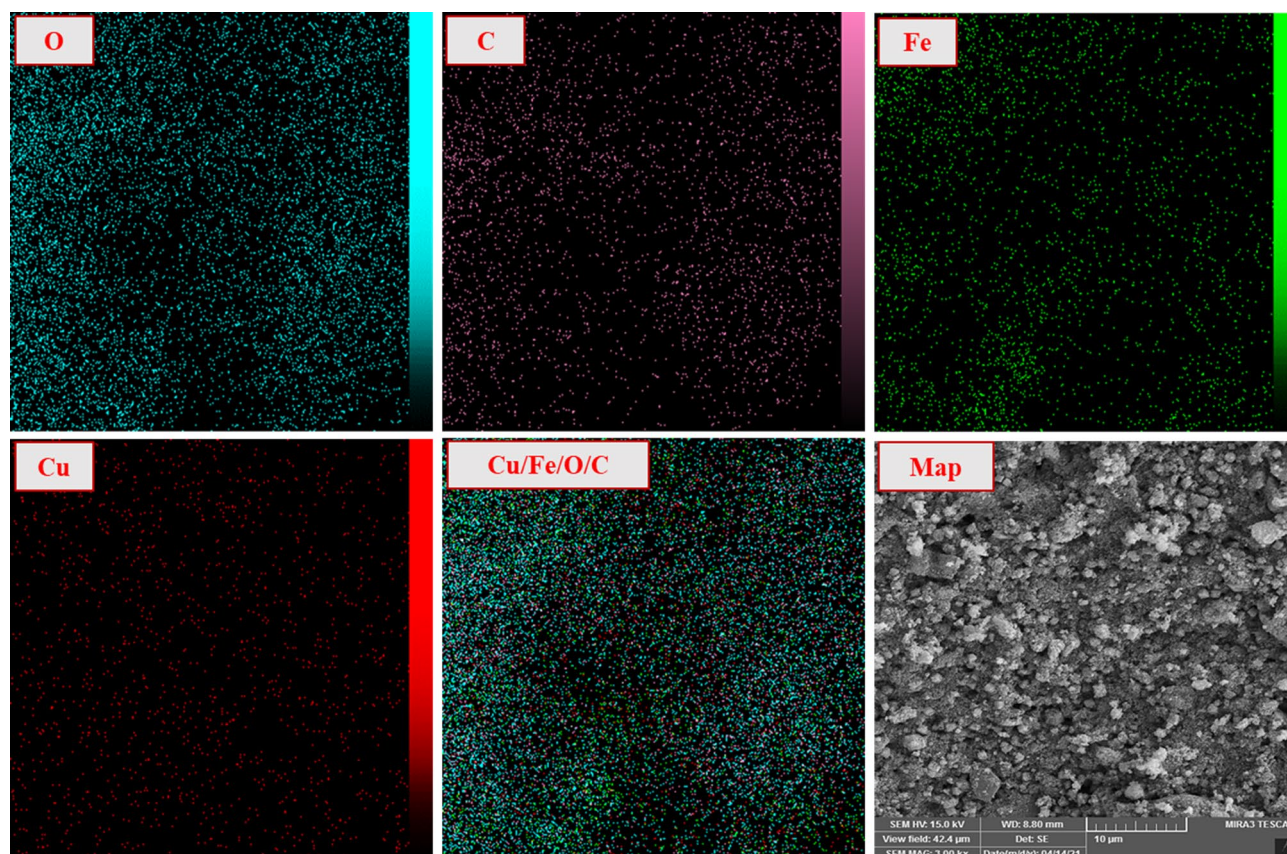


Figure 6. EDS elemental mapping of $\text{CuFe}_2\text{O}_4@\text{CQD}$ nanocomposite.

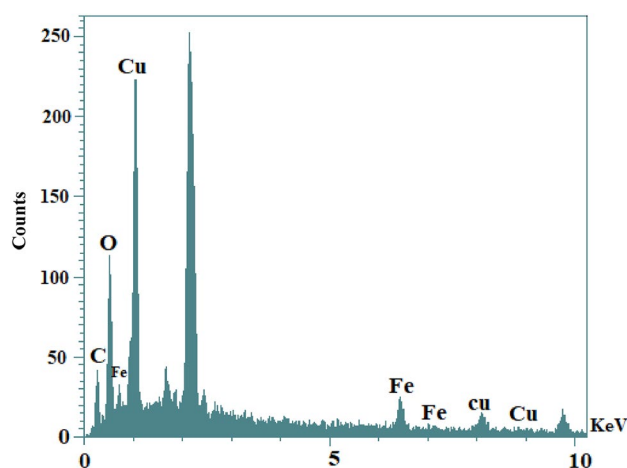


Figure 7. The EDX spectrum of $\text{CuFe}_2\text{O}_4@\text{CQD}$ nanocomposite.

porosity of the synthesized CuFe_2O_4 nanoparticles. Additionally, the mean pore volume of 7.3 nm indicated its nanostructure, as expected.

N_2 adsorption/desorption isotherm of $\text{CuFe}_2\text{O}_4@\text{CQD}$ nanocomposite in P/P_0 ranging from 0 to 1 is presented in Fig. 9a. $\text{CuFe}_2\text{O}_4@\text{CQD}$ nanocomposite indicates the trend classified as II mode, indicative of nanoporous structure. The hysteresis of H4 is obvious for $\text{CuFe}_2\text{O}_4@\text{CQD}$ nanocomposite, indicating slim slit-like pores and wide distribution of irregular internal mesopores in particles. This mode and hysteresis simultaneously reveal the formation of mesopores in the nanoporous $\text{CuFe}_2\text{O}_4@\text{CQD}$ nanocomposite. Figure 9b illustrates the BJH pore size distribution of $\text{CuFe}_2\text{O}_4@\text{CQD}$ nanocomposite at pore diameters ranging from 1 to 100. This curve indicates the wide presence of small-diameter mesopores, minor high-diameter mesopores, and the paucity of macropores in $\text{CuFe}_2\text{O}_4@\text{CQD}$ nanocomposite texture. There is substantial conformity between pore size

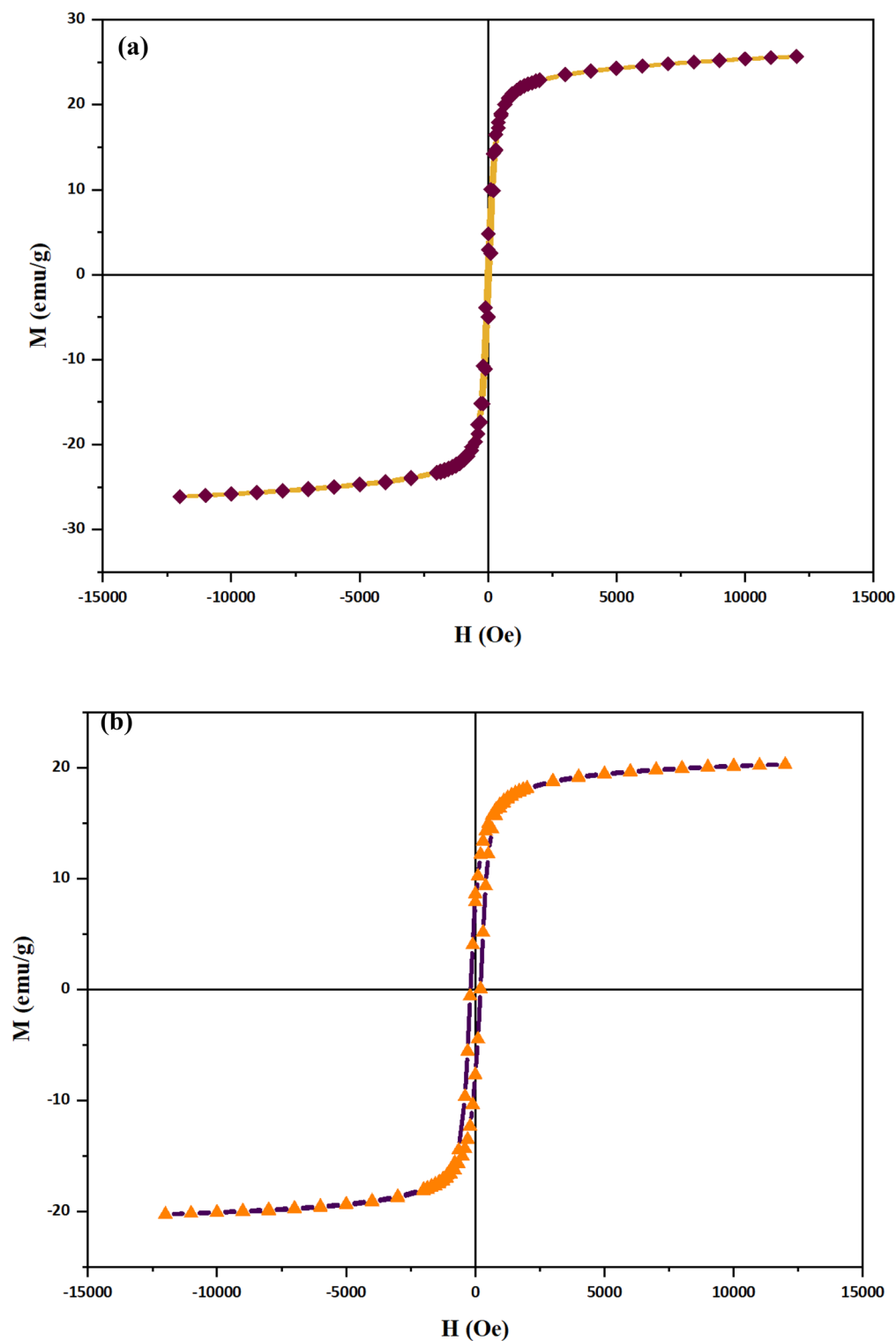


Figure 8. VSM curve of (a) CuFe₂O₄ nanoparticles, (b) CuFe₂O₄@CQD nanocomposite.

Material	BET surface area (m ² /g)	BJH pore volume (cm ³ /g)	Mean pore diameter (nm)
CuFe ₂ O ₄ @CQD nanocomposite	29.5	0.04	5.67
CuFe ₂ O ₄ nanoparticles	110.6	0.25	7.3

Table 1. Structural and textural properties of the prepared materials.

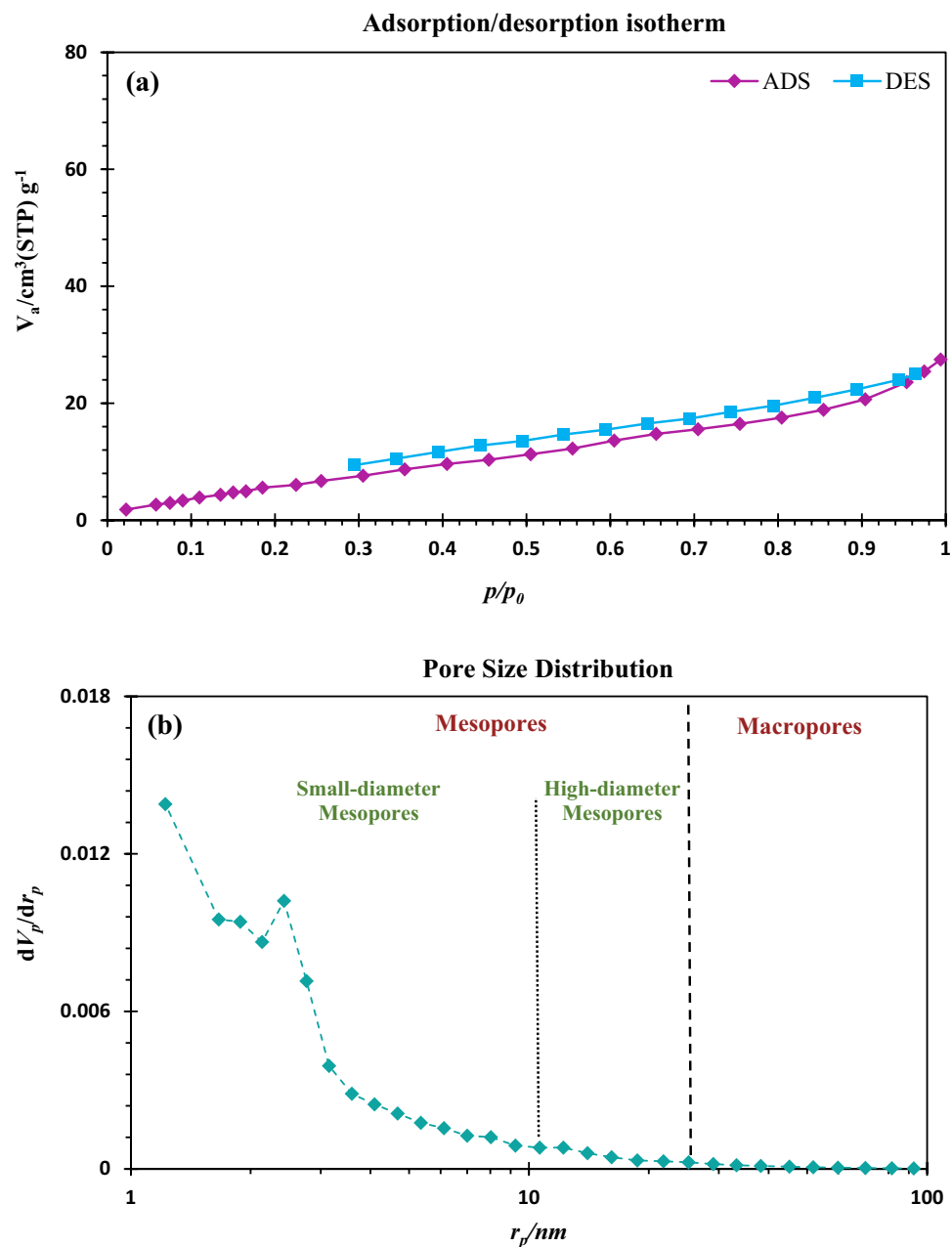


Figure 9. (a) N₂ adsorption/desorption isotherm, (b) pore size distribution curve of CuFe₂O₄/CQD nanocomposite.

distribution and N₂ adsorption/desorption of CuFe₂O₄@CQD nanocomposite, which possesses the nanoporous structure to team with small-diameter mesopores.

The N₂ adsorption/desorption and pore size distribution profile of CuFe₂O₄ NPs are depicted in Fig. 10. Illustrated N₂ adsorption/desorption isotherm of CuFe₂O₄ NPs in P/P₀ ranging from 0 to 1 demonstrates the II mode trend, indicating the formation of nanoporous configuration. Furthermore, the hysteresis of this nanoparticle can be classified as H4, which corroborates the slim slit-like pores and the scattering of inner mesopores in texture. Consequently, based on the reported BJH pore volume profile and N₂ adsorption/desorption plot, it can be concluded that CuFe₂O₄ NPs constitute the mesopores and identifies as the mesoporous configuration. The presented pore volume profile indicates the presence of mesopores, with a pore diameter of less than 50 nm, in the texture of the nanoparticles. Moreover, there is no formation of macropores during the development of corresponding nanoparticles. As a result, this nanoparticle is a mesoporous structure.

Catalytic examinations. The catalytic evaluation was measured by UV-Vis spectroscopy at a wavelength between 250 and 550 nm. To inspect the influence of the obtained nanocatalyst on the reduction of o-NA and p-NA as a sample of regenerative organic matter in the water-based solution, a constant amount of acquired cat-

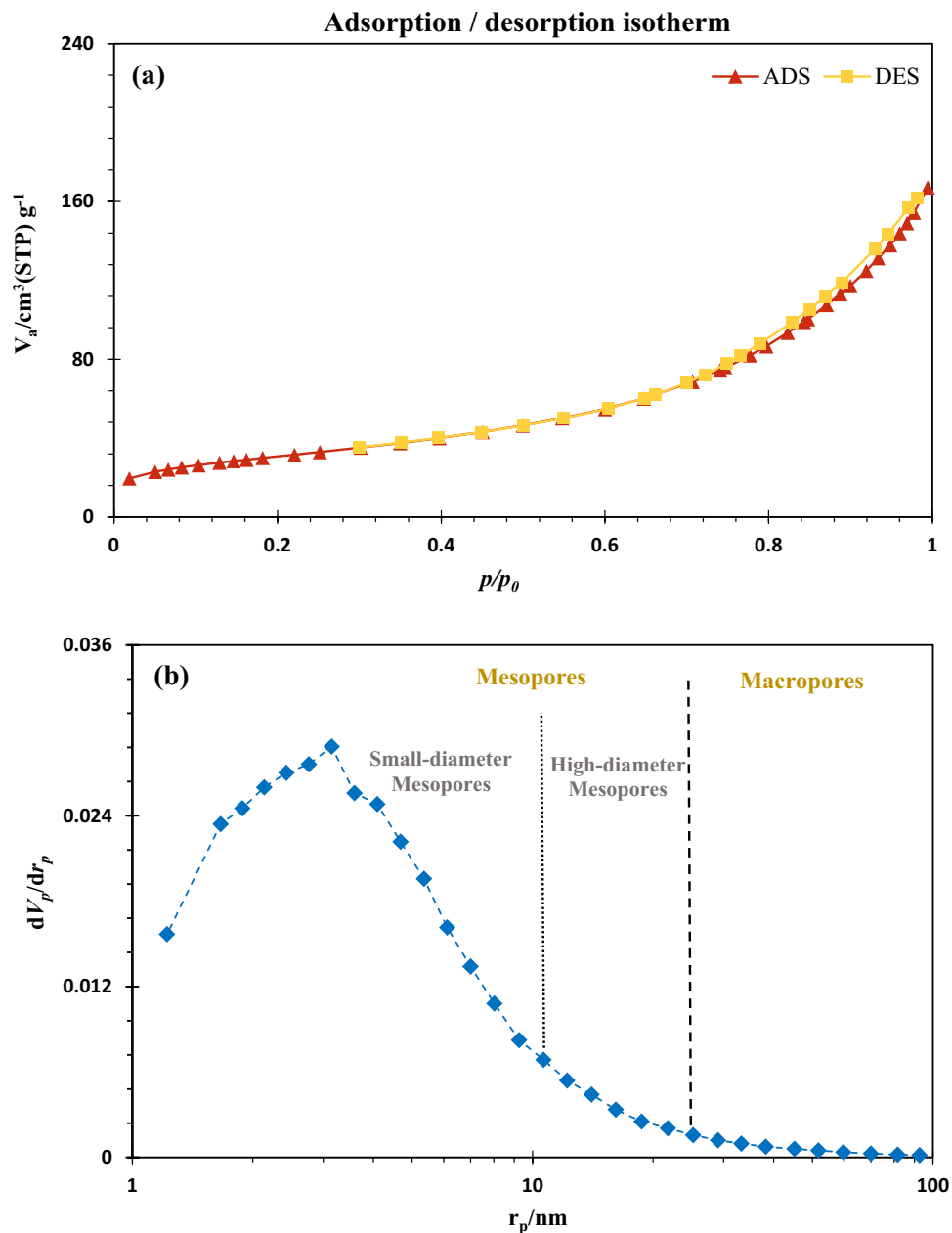


Figure 10. (a) N_2 adsorption/desorption isotherm, (b) pore size distribution curve of $CuFe_2O_4$ nanoparticles.

alyst was added after the addition of $NaBH_4$ as a reducing agent. Subsequently, to acquire the reduction progress, the decrease in absorbance was calculated as a function of the expressed wavelength⁷⁰. In addition, according to Fig. 11, by monitoring the color change of *o*-nitroaniline from orange/yellow to light gray (colorless) during the catalytic reduction, we can easily observe that the *o*-nitroaniline reduction reaction was successfully done. Studies revealed that the main color of *o*-nitroaniline was dark yellow; after adding $NaBH_4$ and nanocatalyst, its color was converted into a colorless solution⁴⁵.

In Fig. 12a, following the addition of the nanocatalyst, adsorption was dropped from about 0.947 to 0.025 at approximately $\lambda_{max} = 415$ nm over 27 s because of the diminishing concentration of *o*-NA. Besides, the elucidated shift from 285 nm to approximately 290 nm can be seen due to the formation of *o*-PDA⁷¹. Figure 12b shows two prominent peaks at 285 and 415 nm ascribed to the *o*-nitroaniline⁷². After adding the fabricated nanocatalyst, by observing a change in the adsorption of *p*-NA, led to the discovery of an effective catalyst that catalyzed *p*-nitroaniline. Moreover, when $CuFe_2O_4@CQD$ nanocomposite was added to the aqueous solution as a catalyst, the adsorption declined from 1.67 to 0.023 at 380 nm within 8 s. The peak, which increased from 0.193 to 0.380 at 307 nm, was attributed to the new product, *para*-PDA.

Considering Fig. 13, at the starting point, *o*-NA, along with $NaBH_4$ as an electron donor (reducer), was adsorbed on the outside of the fabricated nanocatalyst, so metal nanoparticles were charged and intensified

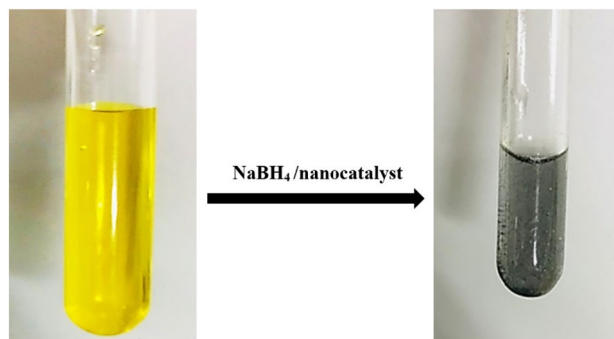


Figure 11. The colour transformation of ortho-nitroaniline after adding the nanocatalyst.

the hydrogenation of o-NA. Thus, the nitroarenes were converted to a nitroso compound and reduced to a hydroxylamine compound. Ultimately, the hydroxylamine composition changed swiftly to the aromatic amine composition⁷³.

One commonly utilized equation for calculating the conversion rate of nanocatalyst is to reduce considered o-nitroaniline to o-phenylenediamine and p-nitroaniline to p-phenylenediamine. The conversion ratio of the reduction reaction of o-NA and p-NA was calculated using Eq. (2)⁷³.

$$\text{Conversion(\%)} = \frac{A_0 - A_t}{A_0} \times 100 \quad (2)$$

where A_0 is the absorbance of o-nitroaniline and p-nitroaniline at the starting time and A_t is the absorbance of nitroaromatics in any time of t .

Evaluate the reduction rate of o-nitroaniline and p-nitroaniline. The concentration of NaBH_4 as a reducing agent is quite higher than the nanocatalyst amount; therefore, the reaction rate relied upon the concentration of o-NA and p-NA. Consequently, the reduction illustrated the first-order kinetics. We utilized Eq. (3) to evaluate the catalytic reduction reaction of ortho-nitroaniline along with para-nitroaniline⁹:

$$\ln\left(\frac{C_t}{C_0}\right) = \ln\left(\frac{A_t}{A_0}\right) = -K_{app} \cdot t \quad (3)$$

where C_t or A_t is the concentration/absorbance measured at time t in the stated wavelength, C_0 or A_0 denote the concentration/absorbance of nitroaromatic at the first time when the reaction was not completely started, and t shows reaction time at any time. K_{app} is the constant rate of nanocatalyst. All the detailed information about the reduction of o-nitroaniline and p-nitroaniline catalyzed by nanocatalyst was calculated and represented in Fig. 14 and Table 2.

In Table 3, the performance of the prepared nanocatalyst was compared to the other recent catalysts. From Table 3, obviously can be seen that the reaction time declined from 90 to 27 s for o-nitroaniline and from 40 to 8 s for p-nitroaniline that indicated that the $\text{CuFe}_2\text{O}_4@\text{CQD}$ (citric acid) surpassed the CuFe_2O_4 nanoparticles. In addition, the apparent constant rate of the reduction reaction for o-nitroaniline and p-nitroaniline was increased from 3.48×10^{-2} to 8.39×10^{-2} and from 7.98×10^{-2} to 5.48×10^{-1} , respectively.

To accurately evaluate the best-fabricated nanocatalyst to catalyze the ortho-NA and para-NA, the $K' = K/m$ formula was used. Where m is considered as the exact amount of used catalyst in the reduction in g or mg and K as the calculated reaction constant rate. As we calculated, the constant rate of $\text{CuFe}_2\text{O}_4@\text{CQD}$ as a nanocatalyst per unit was, $K' = 8.39 \times 10^{-2} \text{ (s}^{-1}\text{)}/3.5 \text{ (mg)}$ and $5.48 \times 10^{-1} \text{ (s}^{-1}\text{)}/3.5 \text{ (mg)}$ for ortho-nitroaniline and para-nitroaniline, sequentially⁷¹.

Analyze the recycle of nanocatalyst. The nanocatalyst's performance was assessed for up to 6 cycles to further evaluate the catalyst's reusability. Regarding this intention, in the first stage, the nanocatalyst was rinsed with ethanol and water after each reduction, and after reaction completion, it was dried utilizing a pump. As shown in Fig. 15, the fabricated catalyst functioned well based on the mentioned response time to reduce o-NA and p-NA. Therefore, during recycling, the catalyst conversion rate in the presence of nanocatalyst decreased from 97.2 to 91.3% for o-nitroaniline and 99.3–93.5 for p-nitroaniline, indicating high usability as well as stability of the prepared catalyst.

Conclusion

As a result, a novel $\text{CuFe}_2\text{O}_4@\text{CQD}$ nanocomposite as a heterogeneous nanocatalyst system was successfully fabricated and characterized. Characterization studies showed that $\text{CuFe}_2\text{O}_4@\text{CQD}$ nanocomposite had cubic and spherical shapes, and their particle size was about 13.5 nm. The catalytic potential of $\text{CuFe}_2\text{O}_4@\text{CQD}$ nanocatalyst was tested with NaBH_4 towards reducing o-NA and p-NA. The catalytic activity of NPs was regenerated

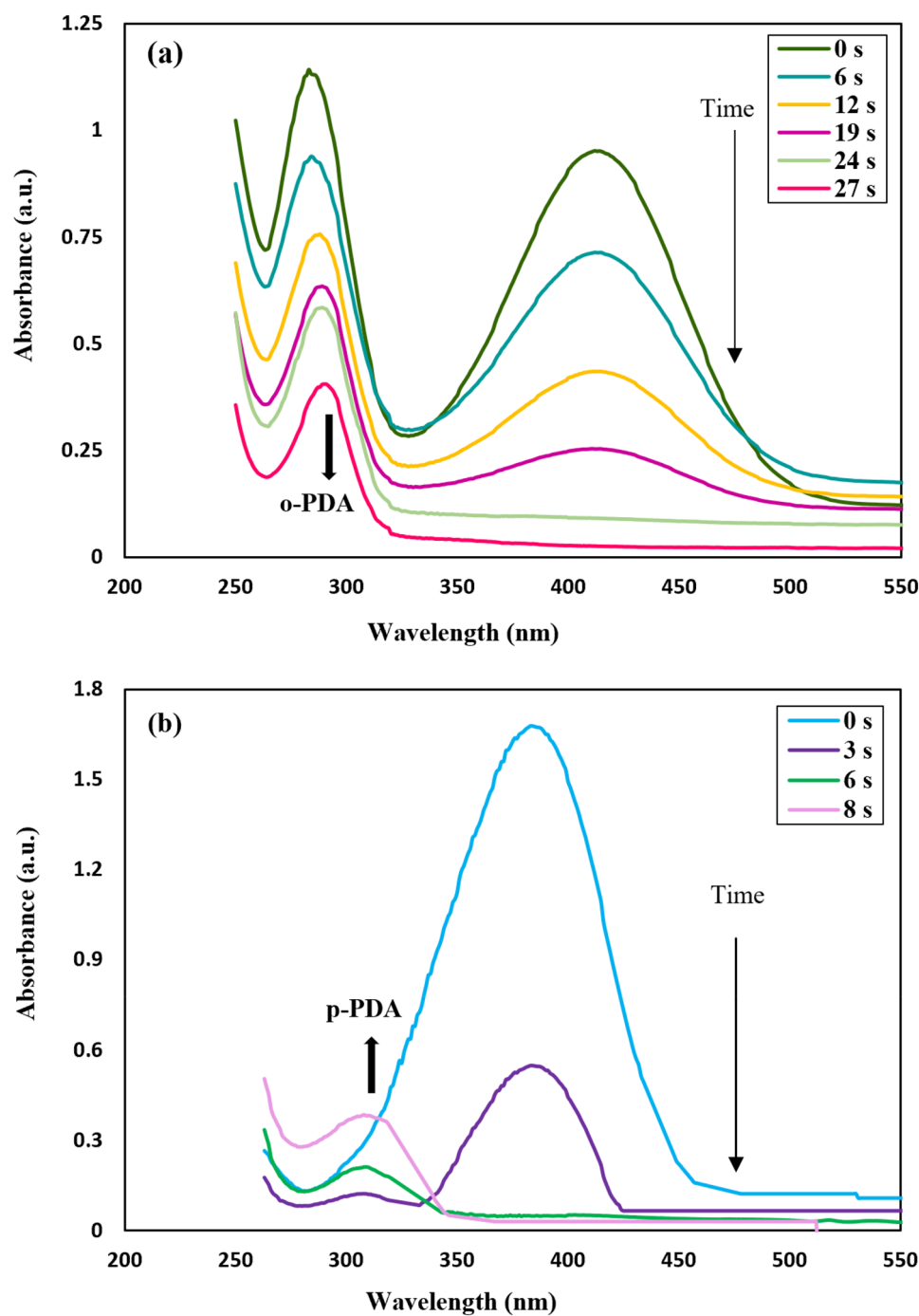


Figure 12. UV-Vis adsorption of (a) o-NA to o-PDA, (b) p-NA to p-PDA; after adding reductant of sodium borohydride and $\text{CuFe}_2\text{O}_4\text{/CQD}$ nanocomposite as a heterogeneous catalyst.

by adding CQDs of citric acid. In addition, the magnetic nanocatalyst converted o-NA to o-phenylenediamine and p-NA to p-phenylenediamine in just 27 and 8 s. Furthermore, it was found that the $\text{CuFe}_2\text{O}_4\text{/CQD}$ nanocatalyst could be reused for up to six cycles.

In summary, the designed catalytic system showed valuable properties such as easy recovery, high stability, easy operation, long life, and excellent catalytic activity in a short reaction time compared to CuFe_2O_4 NPs. These outcomes conclude that $\text{CuFe}_2\text{O}_4\text{/CQD}$ nanocatalyst had promising applications in catalysis, especially for wastewater treatment in the dyeing industry.

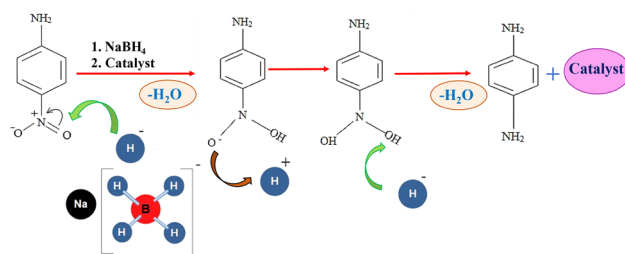


Figure 13. Mechanism of para-nitroaniline catalyzed by the prepared nanocatalyst.

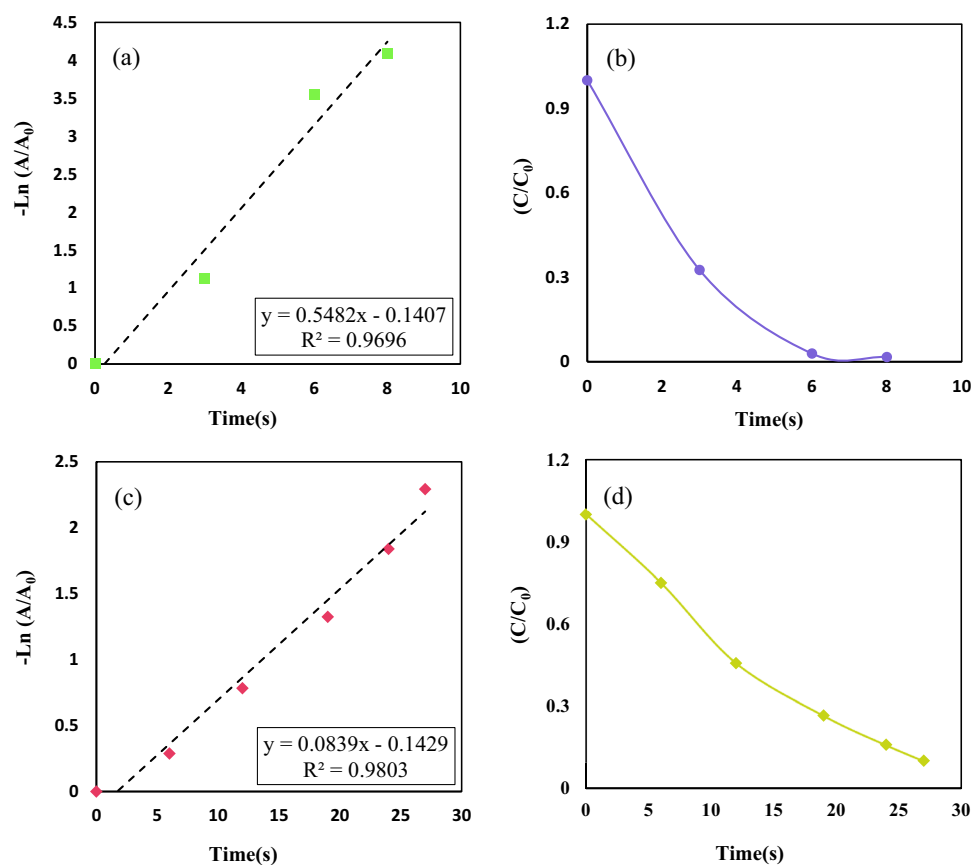


Figure 14. Plots of $-\ln(\frac{A}{A_0})$ vs time for the reduction reaction of (a,b) o-nitroaniline to ortho-PDA, (c,d) p-nitroaniline to para-PDA using prepared nanocatalyst.

Nitroaromatics	Conversion (%)	R ²	K _{app} (s ⁻¹)	Completion time (s)
O-nitroaniline	97.23	0.980	8.39×10^{-2}	27
P-nitroaniline	97.04	0.969	5.48×10^{-1}	8

Table 2. Outcomes of o-NA and p-NA reduction using magnetic nanocatalyst.

Catalyst	Catalyst amount	K_{app} (s^{-1})	Time	Nitroarene	References
20%V dopped-Bi ₂ (O, S) ₃	10 mg	34.4×10^{-3}	150 s	o-Nitroaniline	74
Pd/CoFe ₂ O ₄ /chitosan	4 mg	–	65 s	o-Nitroaniline	45
CoMn ₂ O ₄ /APTOSS@FPS	1 mg	1.83×10^{-2}	100 s	o-Nitroaniline	71
CoMn ₂ O ₄ /APTOSS@FPS	1 mg	1.83×10^{-2}	100 s	o-nitroaniline	71
Au/SiO ₂ -shell/Fe ₃ O ₄ -core	3 mg	4.1×10^{-3}	4.2 min	o-Nitroaniline	72
SiO ₂ @Cu ₂ O@TiO ₂	10 mg	0.018	150 s	o-Nitroaniline	75
Ag NPs	0.50 mL	2.43×10^{-3}	540 s	o-Nitroaniline	76
CeO ₂	0.1 mg	–	60 s	o-Nitroaniline	77
GO/Au	5 mg	5.8×10^{-3}	1320 s	o-Nitroaniline	78
Ag/kcc ⁻¹	10 mg	4.3×10^{-3}	540 s	o-Nitroaniline	79
CuFe ₂ O ₄	3.5 mg	3.48×10^{-2}	90 s	o-Nitroaniline	54
CuFe ₂ O ₄ @CQD (gelatin)	3.5 mg	9.3×10^{-2}	35 s	o-Nitroaniline	80
CuFe ₂ O ₄ @CQD (citric acid)	3.5 mg	8.39×10^{-2}	27 s	o-Nitroaniline	This study
ZnO nanoparticles	10 mg/L	2.44×10^{-2}	105 min	p-Nitroaniline	81
Ni/RGO	10 mg/50 mL	1.29×10^{-2}	190 min	p-Nitroaniline	82
ZnO/CdO/RGO	1.2 mg/L	7.1×10^{-3}	120 min	p-Nitroaniline	83
Ag nanoparticles	4 mg/L	8.52×10^{-1}	13 min	p-Nitroaniline	84
CuFe ₂ O ₄	3.5 mg	7.98×10^{-2}	40 s	p-Nitroaniline	54
CuFe ₂ O ₄ @CQD (gelatin)	3.5 mg	2.89×10^{-1}	13 s	p-Nitroaniline	80
CuFe ₂ O ₄ @CQD (citric acid)	3.5 mg	5.48×10^{-1}	8 s	p-Nitroaniline	This study

Table 3. Comparison of the constant rate of other catalysts used for reduction of o-NA and p-NA.

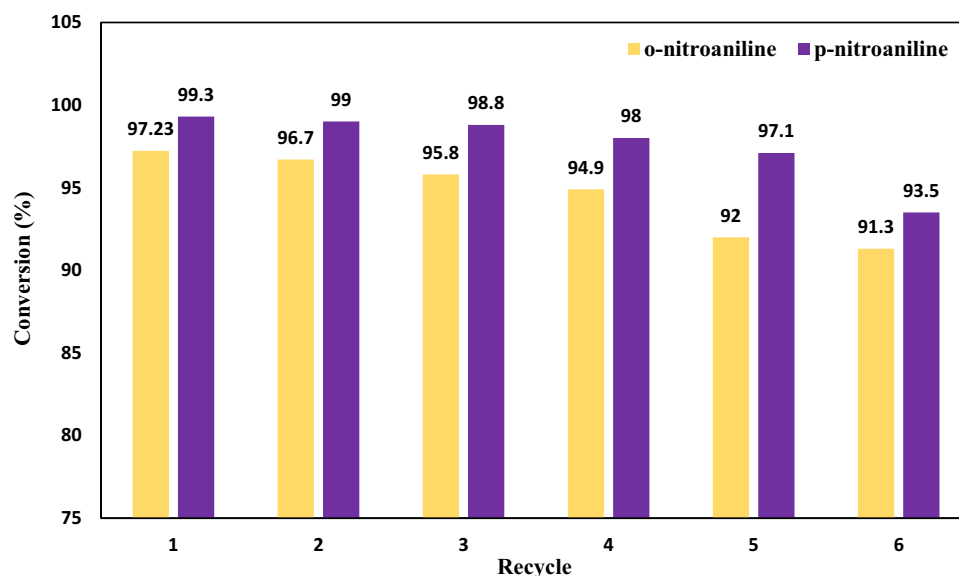


Figure 15. Recycle of nanocatalyst for up to 6 cycles.

Data availability

All data generated or analysed during this study are included in this published article.

Received: 18 October 2022; Accepted: 27 January 2023

Published online: 27 February 2023

References

1. Yadav, D. & Awasthi, S. K. A Pd confined hierarchically conjugated covalent organic polymer for hydrogenation of nitroaromatics: Catalysis, kinetics, thermodynamics and mechanism. *Green Chem.* **22**(13), 4295–4303 (2020).
2. Hu, H., Xin, J. H., Hu, H., Wang, X., Miao, D., & Liu, Y. Synthesis and stabilization of metal nanocatalysts for reduction reactions—a review. *J. Mater. Chem. A* **3**(21), 11157–11182 (2015).

3. Ashrafiava, M., Mousavi, S. B., Heris, S. Z., Heidari, M., Mohammadpourfard, M., & Aslani, H. Investigation of H₂O₂/UV advanced oxidation process on the removal rate of coliforms from the industrial effluent: A pilot-scale study. *Int. J. Hydrogen Energy* **47**(78), 33530–33540 (2022).
4. Heidari, M., Tahmasebpour, M., Antzaras, A. & Lemonidou, A. A. CO₂ capture and fluidity performance of CaO-based sorbents: Effect of Zr, Al and Ce additives in tri-, bi- and mono-metallic configurations. *Process Saf. Environ. Prot.* **144**, 349–365 (2020).
5. Mousavi, S. B., Heidari, M., Rahmani, F., Sene, R. A., Clough, P. T., & Ozmen, S. Highly robust ZrO₂-stabilized CaO nanoadsorbent prepared via a facile one-pot MWCNT-template method for CO₂ capture under realistic calcium looping conditions. *J. Cleaner Prod.* **384**, 135579 (2023).
6. Mal, D., Alveroglu, E., Balouch, A., Jagirani, M. S., Abdullah, & Kumar, S. Highly efficient and selective heterogeneous catalytic reduction of 2-nitroaniline by cerium oxide nanocatalyst under microwave irradiation. *Environ. Technol.* **20**, 1–15 (2021).
7. Farooqi, Z. H., Naseem, K., Begum, R. & Ijaz, A. Catalytic reduction of 2-nitroaniline in aqueous medium using silver nanoparticles functionalized polymer microgels. *J. Inorg. Organomet. Polym. Mater.* **25**(6), 1554–1568 (2015).
8. Ma, J., Gao, M., Shi, H., Ni, J., Xu, Y., & Wang, Q. Progress in research and development of particle electrodes for three-dimensional electrochemical treatment of wastewater: A review. *Environ. Sci. Pollut. Res.* **28**(35), 47800–47824 (2021).
9. Ebratkhan, M., Naghash Hamed, S., Zarei, M., Jafarizad, A. & Rostamizadeh, M. Removal of neutral red dye via electro-fenton process: A response surface methodology modeling. *Electrocatalysis* **12**(5), 579–594 (2021).
10. Pourpasha, H., Farshad, P. & Heris, S. Z. Modeling and optimization the effective parameters of nanofluid heat transfer performance using artificial neural network and genetic algorithm method. *Energy Rep.* **7**, 8447–8464 (2021).
11. Alizadeh, H., Pourpasha, H., Heris, S. Z. & Estellé, P. Experimental investigation on thermal performance of covalently functionalized hydroxylated and non-covalently functionalized multi-walled carbon nanotubes/transformer oil nanofluid. *Case Stud. Thermal Eng.* **31**, 101713 (2022).
12. Moghadam, A. V., Goshayeshi, H. R., Chaer, I., Paurine, A., Heris, S. Z., & Pourpasha, H. Experimental investigation of multiwall carbon nanotubes/water nanofluid pool boiling on smooth and groove surfaces. *Int. J. Energy Res.* **46**(14), 19882–19893 (2022).
13. Kargaran, M., Goshayeshi, H. R., Pourpasha, H., Chaer, I. & Heris, S. Z. An extensive review on the latest developments of using oscillating heat pipe on cooling of photovoltaic thermal system. *Therm. Sci. Eng. Progress* **20**, 101489 (2022).
14. Pourpasha, H., Heris, S. Z. & Mohammadpourfard, M. The effect of TiO₂ doped multi-walled carbon nanotubes synthesis on the thermophysical and heat transfer properties of transformer oil: A comprehensive experimental study. *Case Stud. Thermal Eng.* **20**, 102607 (2022).
15. Pourpasha, H., Heris, S. Z., Mahian, O. & Wongwises, S. The effect of multi-wall carbon nanotubes/turbine meter oil nanofluid concentration on the thermophysical properties of lubricants. *Powder Technol.* **367**, 133–142 (2020).
16. Karimi Shoar, Z., Pourpasha, H., Zeinali Heris, S., Mousavi, S. B., & Mohammadpourfard, M. The effect of heat transfer characteristics of macromolecule fouling on heat exchanger surface: A dynamic simulation study. *Can. J. Chem. Eng.* <https://doi.org/10.1002/cjce.24832> (2023).
17. Pourpasha, H., Heris, S. Z. & Mohammadfam, Y. Comparison between multi-walled carbon nanotubes and titanium dioxide nanoparticles as additives on performance of turbine meter oil nano lubricant. *Sci. Rep.* **11**(1), 1–19 (2021).
18. Heidari, M., Tahmasebpour, M., Mousavi, S. B. & Pevida, C. CO₂ capture activity of a novel CaO adsorbent stabilized with (ZrO₂+ Al₂O₃+ CeO₂)-based additive under mild and realistic calcium looping conditions. *J. CO₂ Util.* **53**, 101747 (2021).
19. Heidari, M., Mousavi, S. B., Rahmani, F., Clough, P. T. & Ozmen, S. The novel Carbon Nanotube-assisted development of highly porous CaZrO₃-CaO xerogel with boosted sorption activity towards high-temperature cyclic CO₂ capture. *Energy Convers. Manage.* **274**, 116461 (2022).
20. Gholami, A., Mousavi, S. B., Heris, S. Z., & Mohammadpourfard, M. Highly efficient treatment of petrochemical spent caustic effluent via electro-Fenton process for COD and TOC removal: optimization and experimental. *Biomass Convers. Biorefin.* 1-17 (2023).
21. Mousavi, S. B., Heris, S. Z. & Estellé, P. Viscosity, tribological and physicochemical features of ZnO and MoS₂ diesel oil-based nanofluids: An experimental study. *Fuel* **293**, 120481 (2021).
22. Mousavi, S. B. & Heris, S. Z. Experimental investigation of ZnO nanoparticles effects on thermophysical and tribological properties of diesel oil. *Int. J. Hydrogen Energy* **45**(43), 23603–23614 (2020).
23. Mousavi, S. B., Heris, S. Z. & Hosseini, M. G. Experimental investigation of MoS₂/diesel oil nanofluid thermophysical and rheological properties. *Int. Commun. Heat Mass Transfer* **108**, 104298 (2019).
24. Sarvari, A. A., Heris, S. Z., Mohammadpourfard, M., Mousavi, S. B. & Estellé, P. Numerical investigation of TiO₂ and MWCNTs turbine meter oil nanofluids: Flow and hydrodynamic properties. *Fuel* **320**, 123943 (2022).
25. Seyedi, S. S., Shabgard, M. R., Mousavi, S. B. & Heris, S. Z. The impact of SiC, Al₂O₃, and B₂O₃ abrasive particles and temperature on wear characteristics of 18Ni (300) maraging steel in abrasive flow machining (AFM). *Int. J. Hydrogen Energy* **46**(68), 33991–34001 (2021).
26. Naghash-Hamed, S., Arsalani, N. & Mousavi, S. B. Facile fabrication of CuFe₂O₄ coated with Carbon Quantum Dots nanocomposite as an efficient heterogeneous catalyst toward the reduction of nitroaniline compounds for management of aquatic resources. *Res. Sq.* <https://doi.org/10.21203/rs.3.rs-2540018/v1> (2023).
27. Padervand, M., Mazloum, M., Bargahi, A. & Arsalani, N. CQDs/BiOCl photocatalysts for the efficient treatment of congo red aqueous solution under visible light. *J. Nanostruct.* **11**(4), 790–801 (2021).
28. Guo, Y., Chen, Y., Hu, X., Yao, Y. & Li, Z. Tween modified CuFe₂O₄ nanoparticles with enhanced supercapacitor performance. *Colloids Surf. A* **631**, 127676 (2021).
29. Rocha, A. K. S., Magnago, L. B., Santos, J. J., Leal, V. M., Marins, A. A. L., Pegoretti, V. C. B., Lelis, M. F. F. & Freitas, M. B. J. G. Copper ferrite synthesis from spent Li-ion batteries for multifunctional application as catalyst in photo Fenton process and as electrochemical pseudocapacitor. *Mater. Res. Bull.* **113**, 231–240 (2019).
30. Liu, J., Xiao, J., Zeng, X., Dong, P., Zhao, J., Zhang, Y., & Li, X. Combustion synthesized macroporous structure MFe₂O₄ (M= Zn, Co) as anode materials with excellent electrochemical performance for lithium ion batteries. *J. Alloy. Compd.* **699**, 401–407 (2017).
31. Astaraki, H., Masoudpanah, S. & Alamolhoda, S. Effects of fuel contents on physicochemical properties and photocatalytic activity of CuFe₂O₄/reduced graphene oxide (RGO) nanocomposites synthesized by solution combustion method. *J. Market. Res.* **9**(6), 13402–13410 (2020).
32. Cui, K., Sun, M., Zhang, J., Xu, J., Zhai, Z., Gong, T., Hou, L. & Yuan, C. Facile solid-state synthesis of tetragonal CuFe₂O₄ spinels with improved infrared radiation performance. *Ceram. Int.* **48**(8), 10555–10561 (2022).
33. Karimpourfard, D., Eslamloueyan, R. & Mehranbod, N. Heterogeneous degradation of stabilized landfill leachate using persulfate activation by CuFe₂O₄ nanocatalyst: An experimental investigation. *J. Environ. Chem. Eng.* **8**(2), 103426 (2020).
34. Rezaie, E., Rezaiezhad, A., Hajalilou, A., Ghadimi, L. S., Abouzari-Lotf, E., & Arsalani, N. Electrochemical behavior of SrFe₁₂O₁₉/CoFe₂O₄ composite nanoparticles synthesized via one-pot hydrothermal method. *J. Alloy. Compd.* **789**, 40–47 (2019).
35. Rezvani, M. A. & Imani, A. Ultra-deep oxidative desulfurization of real fuels by sandwich-type polyoxometalate immobilized on copper ferrite nanoparticles, Fe₆W₁₈O₇₀CuFe₂O₄, as an efficient heterogeneous nanocatalyst. *J. Environ. Chem. Eng.* **9**(1), 105009 (2021).
36. Safartoobi, A., Mazloom, J. & Ghodsi, F. Electrochemical and optical properties of magnetic CuFe₂O₄ nanofibers grown by PVP and PVA-assisted sol-gel electrospinning. *Appl. Phys. A* **128**(1), 1–15 (2022).

37. Selima, S., Khairy, M. & Mousa, M. Comparative studies on the impact of synthesis methods on structural, optical, magnetic and catalytic properties of CuFe₂O₄. *Ceram. Int.* **45**(5), 6535–6540 (2019).
38. Asadian, E., Ghalkhani, M. & Shahrokhian, S. Electrochemical sensing based on carbon nanoparticles: A review. *Sens. Actuators B Chem.* **293**, 183–209 (2019).
39. Cayuela, A., Soriano, M., Carrillo-Carrión, C. & Valcárcel, M. Semiconductor and carbon-based fluorescent nanodots: The need for consistency. *Chem. Commun.* **52**(7), 1311–1326 (2016).
40. Javadpour, R., Heris, S. Z., Mohammadfam, Y. & Mousavi, S. B. Optimizing the heat transfer characteristics of MWCNTs and TiO₂ water-based nanofluids through a novel designed pilot-scale setup. *Sci. Rep.* **12**(1), 1–23 (2022).
41. Yu, J., Zhang, C., Yang, Y., Yi, G., Fan, R., Li, L., Xing, B., Liu, Q., Jia, J. & Huang, G. Lignite-derived carbon quantum dot/TiO₂ heterostructure nanocomposites: Photoinduced charge transfer properties and enhanced visible light photocatalytic activity. *New J. Chem.* **43**(46), 18355–18368 (2019).
42. Dave, K. & Gomes, V. G. Carbon quantum dot-based composites for energy storage and electrocatalysis: mechanism, applications and future prospects. *Nano Energy* **66**, 104093 (2019).
43. Shah, M., Guo, Q.-X. & Fu, Y. The colloidal synthesis of unsupported nickel-tin bimetallic nanoparticles with tunable composition that have high activity for the reduction of nitroarenes. *Catal. Commun.* **65**, 85–90 (2015).
44. Edison, T. N. J. I., Sethuraman, M. G. & Lee, Y. R. NaBH₄ reduction of ortho and para-nitroaniline catalyzed by silver nanoparticles synthesized using *Tamarindus indica* seed coat extract. *Res. Chem. Intermed.* **42**(2), 713–724 (2016).
45. Baran, T. & Nasrollahzadeh, M. Pd/CoFe₂O₄/chitosan: A highly effective and easily recoverable hybrid nanocatalyst for synthesis of benzonitriles and reduction of 2-nitroaniline. *J. Phys. Chem. Solids* **149**, 109772 (2021).
46. Gupta, S. S. R., Kantam, M. L. & Bhanage, B. M. Sha (2019) pe-selective synthesis of gold nanoparticles and their catalytic activity towards reduction of p-nitroaniline. *Nano-Struct. Nano-Objects* **14**, 125–130 (2018).
47. Liu, B., Yang, M. & Li, H. Synthesis of gold nanoflowers assisted by a CH-CF hybrid surfactant and their applications in SERS and catalytic reduction of 4-nitroaniline. *Colloids Surf. A* **520**, 213–221 (2017).
48. Jiji, S. & Gopchandran, K. Shape dependent catalytic activity of unsupported gold nanostructures for the fast reduction of 4-nitroaniline. *Colloid Interface Sci. Commun.* **29**, 9–16 (2019).
49. Revathi, K., Palantavida, S. & Vijayan, B. K. Effective reduction of p-nitroaniline to p-phenylenediamine using Cu–CuO nano-composite. *Mater. Today Proc.* **9**, 633–638 (2019).
50. Mirzaei, A., Janghorban, K., Hashemi, B., Hosseini, S. R., Bonyani, M., Leonardi, S. G., Bonavita, A. & Neri, G. Synthesis and characterization of mesoporous α-Fe₂O₃ nanoparticles and investigation of electrical properties of fabricated thick films. *Process. Appl. Ceram.* **10**(4), 209–217 (2016).
51. Homogen, M. Synthesis and physicochemical properties of magnetite nanoparticles (Fe₃O₄) as potential solid support for homogeneous catalysts. *Malays. J. Anal. Sci.* **22**, 768–774 (2018).
52. Zhang, T. *et al.* Thermal behavior of nitrocellulose-based superthermites: Effects of nano-Fe₂O₃ with three morphologies. *RSC Adv.* **7**(38), 23583–23590 (2017).
53. Amulya, M. S. *et al.* Evaluation of bifunctional applications of CuFe₂O₄ nanoparticles synthesized by a sonochemical method. *J. Phys. Chem. Solids* **148**, 109756 (2021).
54. Naghash-Hamed, S., Arsalani, N. & Mousavi, S. B. The catalytic reduction of nitroanilines using synthesized CuFe₂O₄ nanoparticles in an aqueous medium. *ChemistryOpen* **11**(11), e202200156 (2022).
55. Eniola, J. O., Kumar, R., Mohamed, O. A., Al-Rashdi, A. & Barakat, M. Synthesis and characterization of CuFe₂O₄/NiMgAl-LDH composite for the efficient removal of oxytetracycline antibiotic. *J. Saudi Chem. Soc.* **24**(1), 139–150 (2020).
56. Sarmasti, N., Seyf, J. Y. & Khazaei, A. Synthesis and characterization of [Fe₃O₄@CQDs@Si(CH₂)₃NH₂@CC@EDA@SO₃H]+Cl⁻ and Fe₃O₄@CQDs@Si(CH₂)₃NH₂@CC@EDA@Cu nanocatalysts and their application in the synthesis of 5-amino-1,3-diphenyl-1H-pyrazole-4-carbonitrile and 1-(morpholinol (phenyl) methyl) naphthalen-2-ol derivatives. *Arab. J. Chem.* **14**(3), 103026 (2021).
57. Pimpang, P., Sumang, R. & Chooopun, S. Effect of concentration of citric acid on size and optical properties of fluorescence graphene quantum dots prepared by tuning carbonization degree. *Chiang Mai J. Sci.* **45**(5), 2005 (2018).
58. Martindale, B. C., Hutton, G. A., Caputo, C. A. & Reisner, E. Solar hydrogen production using carbon quantum dots and a molecular nickel catalyst. *J. Am. Chem. Soc.* **137**(18), 6018–6025 (2015).
59. Hao, J., Li, L., Zhao, W., Wu, X., Xiao, Y., Zhang, H., Tang, N. & Wang, X. Carboxyl carbon quantum dots: A novel type of environmental-friendly scale inhibitor. [arXiv:1810.00935](https://arxiv.org/abs/1810.00935) (arXiv preprint) (2018).
60. Rezaezhad, A., Rezaie, E., Ghadimi, L. S., Hajalilou, A., Abouzari-Lotf, E., & Arsalani, N. Outstanding supercapacitor performance of Nd–Mn co-doped perovskite LaFeO₃@ nitrogen-doped graphene oxide nanocomposites. *Electrochim. Acta* **335**, 135699 (2020).
61. Liu, L., Hu, N., An, Y., Du, X., Zhang, X., Li, Y., Zeng, Y. & Cui, Z. Ag₂O and NiO decorated CuFe₂O₄ with enhanced photocatalytic performance to improve the degradation efficiency of methylene blue. *Materials* **13**(21), 4760 (2020).
62. Yan, H., Zhang, Y., Wang, Y., Liu, J., Li, X., Zhang, Y., & Dong, P. Morphology-selected synthesis of copper ferrite via spray drying with excellent sodium storage properties. *Ceram. Int.* **45**(16), 20796–20802 (2019).
63. Cai, Z., Ye, Y., Wan, X., Liu, J., Yang, S., Xia, Y., Li, G. & He, Q. Morphology-dependent electrochemical sensing properties of iron oxide-graphene oxide nanohybrids for dopamine and uric acid. *Nanomaterials* **9**(6), 835 (2019).
64. Plyasova, L. M., Kardash, T. Y., Svintsitskiy, D. A., Paukshtis, E. A., Shterster, N. V., & Minyukova, T. P. The interaction of copper-containing spinels CuFe₂O₄ and CuFeCrO₄ with hydrogen. *Mater. Res. Bull.* **118**, 110481 (2019).
65. Mousavi, S. B., Heris, S. Z. & Estellé, P. Experimental comparison between ZnO and MoS₂ nanoparticles as additives on performance of diesel oil-based nano lubricant. *Sci. Rep.* **10**(1), 1–17 (2020).
66. Sobhani, E., Heris, S. Z. & Mousavi, S. B. The synergistic effect of intumescent fire-resistive paint containing TiO₂ nanoparticles and chlorinated paraffin onto atmospheric-metallic substrates. *ChemistrySelect* **7**(44), e202203513 (2022).
67. Amiri, R., Rezaei, A., Fattahi, N., Pirsahab, M., Rodriguez-Chueca, J., & Moradi, M. Carbon quantum dots decorated Ag/CuFe₂O₄ for persulfate-assisted visible light photocatalytic degradation of tetracycline: A comparative study. *J. Water Process Eng.* **47**, 102742 (2022).
68. Coey, J. M. D. Noncollinear spin arrangement in ultrafine ferrimagnetic crystallites. *Phys. Rev. Lett.* **27**(17), 1140–1142 (1971).
69. Amir, M., Gungunes, H., Slimani, Y., Tashkandi, N., El Sayed, H. S., Aldakheel, F., Sertkol, M., Sozeri, H., Ercan, I. & Baykal, A. Mössbauer studies and magnetic properties of cubic CuFe₂O₄ nanoparticles. *J. Supercond. Novel Magn.* **32**(3), 557–564 (2019).
70. Das, P. & Ghosh, S. Heterogeneous catalytic reduction of 4-nitroaniline by RGO-Ni nanocomposite for water resource management. *J. Mater. Sci. Mater. Electron.* **30**(22), 19731–19737 (2019).
71. Chen, Y., Feng, L. & Sadeghzadeh, S. M. Reduction of 4-nitrophenol and 2-nitroaniline using immobilized CoMn₂O₄ NPs on lignin supported on FPS. *RSC Adv.* **10**(33), 19553–19561 (2020).
72. Bhaduri, K., Das, B. D., Kumar, R., Mondal, S., Chatterjee, S., Shah, S., Bravo-Suárez, J. J. & Chowdhury, B. Recyclable Au/SiO₂-shell/Fe₃O₄-core catalyst for the reduction of nitro aromatic compounds in aqueous solution. *ACS Omega* **4**(2), 4071–4081 (2019).
73. Sundarapandi, M., Viswanathan, P., Sivakumar, S. & Ramaraj, R. Catalytic activities of mono- and bimetallic (Gold/Silver) nanoshell-coated gold nanocubes toward catalytic reduction of nitroaromatics. *Langmuir* **34**(46), 13897–13904 (2018).
74. Abay, A. K., Kuo, D.-H., Chen, X. & Saragih, A. D. A new V-doped Bi₂(O, S)₃ oxysulfide catalyst for highly efficient catalytic reduction of 2-nitroaniline and organic dyes. *Chemosphere* **189**, 21–31 (2017).

75. Zelekew, O. A. & Kuo, D.-H. Facile synthesis of $\text{SiO}_2@\text{Cu}_x\text{O}@\text{TiO}_2$ heterostructures for catalytic reductions of 4-nitrophenol and 2-nitroaniline organic pollutants. *Appl. Surf. Sci.* **393**, 110–118 (2017).
76. Edison, T. N. J. I., Sethuraman, M. G. & Lee, Y. R. NaBH_4 reduction of ortho and para-nitroaniline catalyzed by silver nanoparticles synthesized using *Tamarindus indica* seed coat extract. *Res. Chem. Intermed.* **42**(2), 713–724 (2016).
77. Mal, D., Alveroglu, E., Balouch, A., Jagirani, M. S. & Abdullah, S. K. Highly efficient and selective heterogeneous catalytic reduction of 2-nitroaniline by cerium oxide nanocatalyst under microwave irradiation. *Environ. Technol.* **20**, 1–31 (2021).
78. Naem, H., Ajmal, M., Muntha, S., Ambreen, J. & Siddiq, M. Synthesis and characterization of graphene oxide sheets integrated with gold nanoparticles and their applications to adsorptive removal and catalytic reduction of water contaminants. *RSC Adv.* **8**(7), 3599–3610 (2018).
79. Dong, Z., Le, X., Li, X., Zhang, W., Dong, C., & Ma, J. Silver nanoparticles immobilized on fibrous nano-silica as highly efficient and recyclable heterogeneous catalyst for reduction of 4-nitrophenol and 2-nitroaniline. *Appl. Catal. B* **158**, 129–135 (2014).
80. Naghash-Hamed, S., Arsalani, N. & Mousavi, S. B. Facile copper ferrite/carbon quantum dot magnetic nanocomposite as an effective nanocatalyst for reduction of para-nitroaniline and ortho-nitroaniline. *Nano Futures* **6**(4), 045003 (2022).
81. Malakootian, M., Khatami, M., Mahdizadeh, H., Nasiri, A. & AmiriGharaghani, M. A study on the photocatalytic degradation of p-Nitroaniline on glass plates by Thermo-Immobilized ZnO nanoparticle. *Inorgan. Nano-Metal Chem.* **50**(3), 124–135 (2020).
82. Das, P., Ghosh, S. & Sen, M. B. Heterogeneous catalytic reduction of 4-nitroaniline by RGO-Ni nanocomposite for water resource management. *J. Mater. Sci. Mater. Electron.* **30**(22), 19731–19737 (2019).
83. Mirzazadeh, H. & Lashanizadegan, M. ZnO/CdO/reduced graphene oxide and its high catalytic performance towards degradation of the organic pollutants. *J. Serb. Chem. Soc.* **83**(2), 221–236 (2018).
84. Farooqi, Z. H., Khalid, R., Begum, R., Farooq, U., Wu, Q., Wu, W., Ajmal, M., Irfan, A. & Naseem, K. Facile synthesis of silver nanoparticles in a crosslinked polymeric system by in situ reduction method for catalytic reduction of 4-nitroaniline. *Environ. Technol.* **40**(15), 2027–2036 (2019).

Author contributions

S.N.-H.: investigation, conceptualization, methodology, formal analysis, writing original draft. N.A.: supervision. S.B.M.: formal analysis, writing original draft.

Competing interests

The authors declare no competing interests.

Additional information

Correspondence and requests for materials should be addressed to N.A. or S.B.M.

Reprints and permissions information is available at www.nature.com/reprints.

Publisher's note Springer Nature remains neutral with regard to jurisdictional claims in published maps and institutional affiliations.



Open Access This article is licensed under a Creative Commons Attribution 4.0 International License, which permits use, sharing, adaptation, distribution and reproduction in any medium or format, as long as you give appropriate credit to the original author(s) and the source, provide a link to the Creative Commons licence, and indicate if changes were made. The images or other third party material in this article are included in the article's Creative Commons licence, unless indicated otherwise in a credit line to the material. If material is not included in the article's Creative Commons licence and your intended use is not permitted by statutory regulation or exceeds the permitted use, you will need to obtain permission directly from the copyright holder. To view a copy of this licence, visit <http://creativecommons.org/licenses/by/4.0/>.

© The Author(s) 2023